

## Synthesis, Corrosion Inhibition Efficiency in Acidic Media, and Quantum Chemical Studies of Some Hydrazone Derivatives

Huda Saleh Abood<sup>1</sup>, Ekhlas Qanber Jasim<sup>2</sup>, Munther Abduljaleel Muhammad-Ali<sup>3\*</sup>

<sup>1</sup>Department of Pharmaceutical Chemistry, College of Pharmacy, University of Basrah, Basra, 61004, Iraq

<sup>2</sup>Department of Pathological Analyses, College of Science, University of Basrah, Basra, 61004, Iraq

<sup>3</sup>Department of Ecology, College of Science, University of Basrah, Basra, 61004, Iraq

\*Corresponding author: munther.ali@uobasrah.edu.iq

### Abstract

In this work, four hydrazone Schiff base derivatives N-(2,4-Dinitro-phenyl)-N'-(1H-pyrrol-2-ylmethylene)-hydrazine (1a), N-Benzo [1,3] dioxol-5-ylmethylene-N'-(2,4-dinitro-phenyl)- hydrazine (1b), (E)-5-((2-(2,4-dinitrophenyl)hydrazono)methyl)-2-hydroxybenzoic acid (1c) and (E)-1-(2,4-dinitrophenyl)-2-(2-methoxybenzylidene)hydrazine (1d) were synthesized by reaction of four aldehydes namely pyrrole-2-carboxaldehyde, piperonal, 5-formylsalicylic acid, and o-vanillin with 2,4-dinitrophenyl hydrazine to produce the final compounds 1a, 1b, 1c, and 1d, respectively. These four compounds were investigated as corrosion inhibitors in aqueous mild acidic static solution. FTIR, HNMR, and elemental analysis were used to elucidate the chemical structure of the synthesized inhibitors. Using potential dynamic polarization measurements, these inhibitors' efficiency in preventing C-steel corrosion in 1.00 M HCl was studied. The results of the experiments revealed that  $1 \times 10^{-3}$  M is the ideal concentration for 1a, 1b, 1c, and 1d, and that the corresponding inhibition efficiencies for these subunits were 80.70%, 91.30%, 91.34, and 88.80%, respectively. The best corrosion inhibitors were compounds 1b and 1c. Furthermore, studies suggested that these substances are mixed-type inhibitors and that the efficiency of the inhibition is strongly correlated with their quantity. Quantum parameters included Dipole moment, energy band gap ( $\Delta E$ ), value of energy of lowermost unoccupied molecular orbital ( $E_{LUMO}$ ), and energy of high most occupied molecular orbital ( $E_{HOMO}$ ) using Molecular Operating Environment MOE, Gaussian, and HyperChem software packages were determined which demonstrated strong agreement between algorithmic and practical findings.

### Keywords

Hydrazone, MOE, Tafel Plot, Dipole Moment

Received: 6 September 2023, Accepted: 25 December 2023

<https://doi.org/10.26554/sti.2024.9.1.137-147>

## 1. INTRODUCTION

Inhibitors of acidity are applied to prevent corrosion of the base metal. One of the biggest issues with industrial processes is the use of additive compounds as corrosion of materials. Corrosion is an unfavorable process that occurs when metals or alloys react with their environment, changing the properties of the material and leading to significant financial losses. Industrial metal buildings are frequently exposed to elements that encourage corrosion processes (Al-Amiery et al., 2023; Chen et al., 2022). In the industrial world, acid solutions are frequently utilized in procedures including Chemical cleaning, acidity of oil wells, and acid treatment of iron and steel. Because it is more affordable and hassle-free than other mineral acids, hydrochloric acid is commonly used. The cathodic reaction and metal dissolution are both controlled by organic corrosion inhibitors, which function as mixed inhibitors. As

a result, they slow down corrosion and keep it under control (Argyropoulos et al., 2021).

According to classification, hydrazones fall under the Schiff base group. It is frequently utilized as an antimicrobial agent. Anti-inflammatory, antitumor, anticancer, and anti-seizure drugs in pharmaceutical chemistry (Sharma et al., 2020). The azomethine group  $R_1R_2-C=NNH-Ph$  found in hydrazones has two distinct functional groups,  $R_1$  and  $R_2$  (Raczuk et al., 2022). The terminal nitrogen atom's lone pair of electrons can conjugate with the azomethine bond. The physical and molecular characteristics of hydrazones are significantly influenced by their nitrogen and carbon atoms. While C is both electrophile and nucleophile, N is a nucleophile (Adam et al., 2023). Because they can create stable metal chelates with all transition metals, hydrazones are crucial in the bioinorganic area in addition to their biological significance (Jabeen, 2022). To safeguard a wide range of metals and alloys, numerous trial

investigations have been carried out recently to produce corrosion inhibitors based on hydrazones formed from different types of aldehydes and organic hydrazine molecules (Maniak et al., 2021; Lgaz et al., 2019).

On the other hand, many researchers supplemented experimental findings with computational calculations, mostly using for simulations of molecular dynamics (MD) and density functional theory, as a result of extensive research in this field (Mazlan et al., 2022; Obot et al., 2022; Muhammad et al., 2020). These investigations frequently center on identifying molecule electronic characteristics and how they relate to experimental effectiveness. A strong association between these characteristics and the effectiveness of the experiment was discovered in many works (Oyeneyin et al., 2022; Hassan et al., 2023).

The aforementioned facts served as our inspiration for this report. The aim of this work was using four hydrazone compounds as novel corrosion inhibitors for carbon steel in HCl 1.00 M at ambient temperature. The use of HCl 1.00 M as an intermediate can provide some initial context for the chemicals under study. Corrosion inhibition characteristics under various operating conditions, even though a higher concentration of hydrogen chloride is commonly used for practical uses. So, Measurements of potentiodynamic polarization were utilized to look at the anti-corrosion capabilities of the present compounds at three distinct doses. Furthermore, Quantum chemical calculations by MOE, Gaussian, and HyperChem programs were used to provide insight into how hydrazone molecules interact with the iron surface through *HOMO*, *LUMO*,  $\Delta E$ , and dipole moment  $\mu$  parameters.

## 2. EXPERIMENTAL SECTION

### 2.1 Materials

The materials 2,4-dinitrophenyl hydrazine, pyrrole-2-carboxaldehyde, piperonal, 5-formyl salicylic acid, and o-vanillin were purchased from Merck and Fluka, and ethyl acetate acquired via Sigma-Aldrich. Solvents from Merck Without additional the process of purification, they were used. The chemical liquid was distilled before use. Uncorrected melting points were measured using a Gallenkamp Thermal Point instrument. Infrared The compounds' spectra were collected in the 4000–400  $\text{cm}^{-1}$  region. using Shimadzu FTIR–8400 spectrophotometer applying the KBr disc technique. The  $^1\text{H}$ NMR spectra were recorded by spectrometer Inova 500 MHz at University of Tehran, Iran. Using a CHN elemental analyzer flash EA 1112 series, synthetic substances underwent elemental microanalysis (CHN) (Thermo finnigan).

### 2.2 Chemistry

#### 2.2.1 Synthesis (1a) N-(2,4-Dinitro-phenyl)-N'-(1H-pyrrol-2-ylmethylene)-hydrazine

A solution of 2,4-dinitrophenyl hydrazine 1.9 g (0.01 mol) in ethyl alcohol 25 mL was added to a 100 mL round-bottom container containing a solution of ethyl alcohol containing 0.98 g (0.01 mol) of pyrrole-2-carboxaldehyde. flask, Figure 1. The

reaction was refluxed with a stirrer for 2 h and under TLC's observation. After cooling the mixture for a whole night, the precipitate was removed, dried, and then crystallized again as of the methanol (Jasim et al., 2023). Table one displays the product's physical attributes. (1a): Marron-colored crystal with an 88% yield and a melting point between 298 and 300 degrees Celsius, and the following infrared spectrum (KBr):  $\nu$  ( $\text{cm}^{-1}$ ) = 3425 (N–H), 3271 (N–H pyrrole ring), 3105 (C–H, Aromatic), 1612 (C=N), 1581 (C=C), 1508, 1327 (NO).  $^1\text{H}$ NMR ( $\text{DMSO}_{d6}$ ):  $\delta$  = 11.69 (s, H, NH), 11.58 (s, H, NH pyrrole), 8.51 (s, H, CH=N), 8.85 (d,  $J$ =2.6 Hz, 1H,  $A_r$ (C–H<sub>a</sub>), 8.31 (dd,  $J$ =9.7, 2.6 Hz, H,  $A_r$ (C–H<sub>b</sub>), 8.18 (d,  $J$ =9.7, H,  $A_r$ (C–H<sub>c</sub>), 7.05 (s, H, pyrrole-H<sub>d</sub>), 6.53 (s,H, pyrrole-H<sub>f</sub>), 6.18 (s, H, pyrrole-H<sub>e</sub>). Anal. Calc. (Found) for  $\text{C}_{11}\text{H}_9\text{N}_5\text{O}_4$  (275.22): C, 48.00 (47.87); H, 3.30 (3.22); N, 25.45 (25.28).

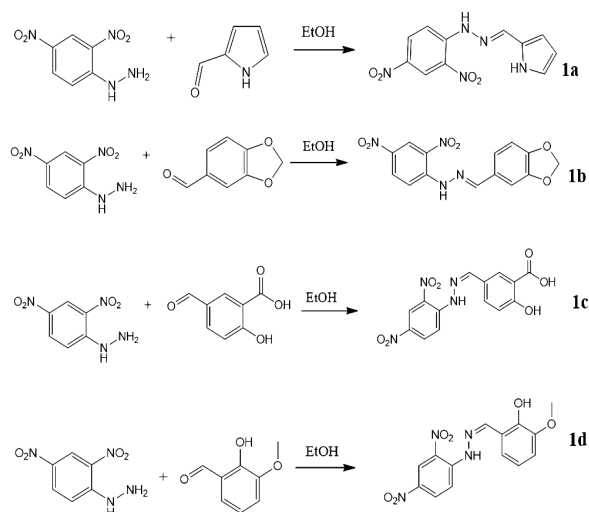


Figure 1. Synthesis of Schiff Bases 1a, 1b, 1c, and 1d

#### 2.2.2 Synthesis of compound (1b) N-benzo [1,3] dioxol-5-ylmethylene-N'-(2,4-dinitro-phenyl)- hydrazine

A solution of 2,4-dinitrophenyl hydrazine (1.9 g, 0.01 mol) stirred in ethyl alcohol 30 mL was mixed in piperonal (1.5 g) in 100 mL round bottom flask, Figure 1. TLC was used to track the reaction while it was refluxed with stirring for one hour. Following an overnight cooling period, the precipitate was filtered, dried out, and obtained by methanol recrystallization (Muhammad-Ali et al., 2023). Table 1 displays the products' physical attributes. (1b): Crystal in a red color, with a yield of 60%, melting point in the range of 264–266 degrees Celsius, and the following IR (KBr) spectrum:  $\nu$  ( $\text{cm}^{-1}$ ) = 3421 (N–H), 3050 (C–H, aromatic), 2951 (C–H, aliphatic), 1620 (C=N, azomethine), 1589 (C=C), 1454, 1390 (N–O), 1261, 1134 (C–O).  $^1\text{H}$  nuclear magnetic resonance ( $\text{DMSO}_{d6}$ ):  $\delta$  (ppm) = 11.61 (s, 1H, NH), 8.60 (s, 1H, CH=N), 8.85 (d,  $J$ =2.6 Hz, 1H,  $A_r$ -H<sub>a</sub>), 8.33 (dd,  $J$ =9.7, 2.6 Hz, 1H,  $A_r$ -H<sub>b</sub>), 8.18 (d,  $J$ =9.3 Hz, 1H,  $A_r$ -H<sub>c</sub>), 7.45 (s, 1H, benzodioxole-H<sub>f</sub>), 7.19 (d,  $J$ =8.0 Hz, 1H, benzodioxole-H<sub>e</sub>), 7.02 (d,  $J$ =7.9 Hz, 1H,

benzodioxole- $H_d$ ), 6.11 (s, 2H, benzodioxole- $CH_2$ -). Anal. Calc. (Found) for  $C_{14}H_{10}N_4O_6$  (330.26): C, 50.92 (50.71); H, 3.05 (3.09); N, 16.97 (17.02).

### 2.2.3 Synthesis of compound (1c) (E)-5-((2-(2,4-dinitrophenyl)hydrazono)methyl)-2-hydroxybenzoic acid

A mixture of 2,4-dinitrophenyl hydrazine (1.9 g, 0.01 mole) and 5-formylsalicylic acid (1.6 g) was agitated in 25 mL of ethanol in a hundred mL circular flask (Figure 1). The resulting precipitate was filtered and refined using methanol recrystallization. (Jasim et al., 2020). Table 1 displays the product's physical characteristics. (1c) Orange-colored crystal with a yield ratio of 65%, a melting point of 236-238 degrees Celsius, and the infrared wavelengths shown below:  $\nu$  ( $cm^{-1}$ ) = 3400 (N-H / O-Overlap), 3117 (C-H, arom.), 1666 (C=O), 1620 (C=N), 1504 (C=C), 1438, 1385 (N-O), 1262 (C-O).  $^1H$ NMR (DMSO- $d_6$ ):  $\delta$  = 11.60 (s, H, NH), 8.64 (s, H, HC=N), 8.85 (d,  $J=2.7$ , H,  $Ar$ (C- $H_a$ )), 8.37 (dd,  $J=8.4$ , 2.7, H,  $Ar$ (C- $H_b$ )), 7.98 (d,  $J=8.4$  H,  $Ar$ (C- $H_c$ )), 8.10 (s, H, salicylic ring- $H_f$ ), 8.04 (d,  $J=9.2$  H, salicylic ring- $H_d$ ), 7.07 (d,  $J=9.2$ , H, salicylic ring- $H_e$ ). Anal. Calc. (Found) for  $C_{14}H_{10}N_4O_7$  (346.26): C, 48.56 (48.29); H, 2.91 (2.94); N, 16.18 (16.09).

### 2.2.4 Synthesis of compound (1d) (E)-1-(2,4-dinitrophenyl)-2-(2-methoxybenzylidene)hydrazine

An ethanolic solution of o-vanillin (1.5 g) in a 100 mL round bottom container was mixed with a solution of 2,4-dinitrophenyl hydrazine (1.9 g, 0.01 mole) agitated in ethanol (20 mL). flask, Figure 1. The reaction was refluxed with a stirrer for 1 h and monitored by TLC. At the end of reaction, the mixture was cooled overnight. The product was filtered and purified by recrystallization from methanol (Parvarinezhad and Salehi, 2021). Table 1 displays the product's physical characteristics. (1d): Crystal in a yellow color, with a yield of 83%, melting point in the range of 242-244 degrees Celsius, and the following IR (KBr) spectrum:  $\nu$  ( $cm^{-1}$ ) = 3400 (N-H), 3290 (OH), 3120 (CH, aromatic), 2935 (CH aliphatic), 1616 (C=N), 1516 (C=C), 1477, 1327 (NO), 1261 (CO).  $^1H$ NMR (DMSO- $d_6$ ):  $\delta$  = 11.73 (s, H, NH), 9.52 (s, H, O-H), 8.99 (s, H, HC=N), 8.86 (d,  $J=3.1$ , H,  $Ar$ (C- $H_a$ )), 8.36 (dd,  $J=9.7$ , 3.1, H,  $Ar$ (C- $H_b$ )), 8.03 (d,  $J=9.5$ , H,  $Ar$ (C- $H_c$ )), 7.44 (d,  $J=7.9$ , H, vanillin ring- $H_d$ ), 7.04 (d,  $J=7.9$ , H, vanillin ring- $H_f$ ), 6.86 (t,  $J=8.0$ , 1H, vanillin ring- $H_e$ ), 3.83 (s, 3H, -OCH $_3$ ). Anal. Calc. (Found) for  $C_{14}H_{12}N_4O_6$  (332.27): C, 50.61 (50.52); H, 3.64 (3.58); N, 16.86 (16.82).

### 2.2.5 Corrosion Study

by adding distilled water to AR grade 37% HCl dilution. A fixed quantity of each molecule was dissolved in 0.5 M HCl to provide the concentrations of  $1 \times 10^{-3}$ ,  $1 \times 10^{-4}$ , and  $1 \times 10^{-5}$  M for the different synthesized compounds.

A model MLab 200 from the Education Faculty of Pure Sciences' Chemistry Department was used for polarization experiments at Basrah University. Tafel polarization was created by automatically varying the electrode potential from (+250

mV to -250 mV) at open circuit potential with a scan rate of 0.5 mV  $S^{-1}$  to investigate the inhibitor's impact on mild steel corrosion. By extending the linear Tafel segments of the cathodic and anodic curves to the corrosion potential ( $I_{corr}$ ), the corrosion current densities were computed. From the computed  $I_{corr}$  values, the inhibition efficiency was determined using Equation 1 (Jasim et al., 2017; Deaf et al., 2022; Njong et al., 2018).

$$E\% = \left[ \frac{I_{corr} - I_{corr(inh)}}{I_{corr}} \right] \times 100\% \quad (1)$$

where  $I_{corr}$  is the corrosion current in the absence of the inhibitors (synthesized compounds) and  $I_{corr(inh)}$  is the corrosion flow when the inhibitors are in place.

### 2.2.6 Computation of Quantum Chemical Parameters

The semi-empirical AM1 method from the MOE 2015 v10 software package, Gaussian09, and HyperChem08 were used to perform quantum chemistry calculations. The Restricted-Hartree-Fock (RHF) level was used to fully optimize every geometrical variable without imposing any symmetry restrictions. To the gradient of 0.01 in the vacuum phase, molecular architectures were tuned.

## 3. RESULTS AND DISCUSSION

### 3.1 Chemistry

The synthesis of the products (1a, 1b, 1c, and 1d) were achieved by condensation of 2,4-dinitrophenyl hydrazine compound with four types of aldehydes (pyrrole-2-carboxaldehyde, piperonal, 5-formylsalicylic acid or o-vanillin), respectively, using refluxed ethanol solvent. The resulting compounds were synthesized with different product yields, components 1a and 1d gave good yields (88 and 83%, respectively) whereas compounds 1b and 1c gave yield of 60 and 65%, respectively, as shown in Table 1.

The resulting compounds were analyzed using IR spectroscopy, revealing significant absorption bands at about 3400  $cm^{-1}$  and roughly 1600  $cm^{-1}$ , which corresponded to the vibrations of a stretch of N-H and C=N, of hydrazone fragment for all synthesized compounds. All compounds showed significant strong bands at the range 1508-1438 and 1390-1327  $cm^{-1}$  attributed to asymmetrical as well as symmetrical stretching vibration, respectively, of nitro groups (Vhanale et al., 2019), as shown in Figures 2 and 3. Compound 1a gave medium band at 3271  $cm^{-1}$  attributed to stretching quivering of pyrrole NH. Compounds 1b as well as 1d reported small regions with stretching vibration at 2951 and 2935  $cm^{-1}$ . of aliphatic C-H for - $CH_2$ - and -OCH $_3$  groups, respectively. Compound 1c revealed a solid band that indicated extending about 1666. vibration of carbonyl group for salicylic fragment (Zhang et al., 2019), as shown in Table 2.

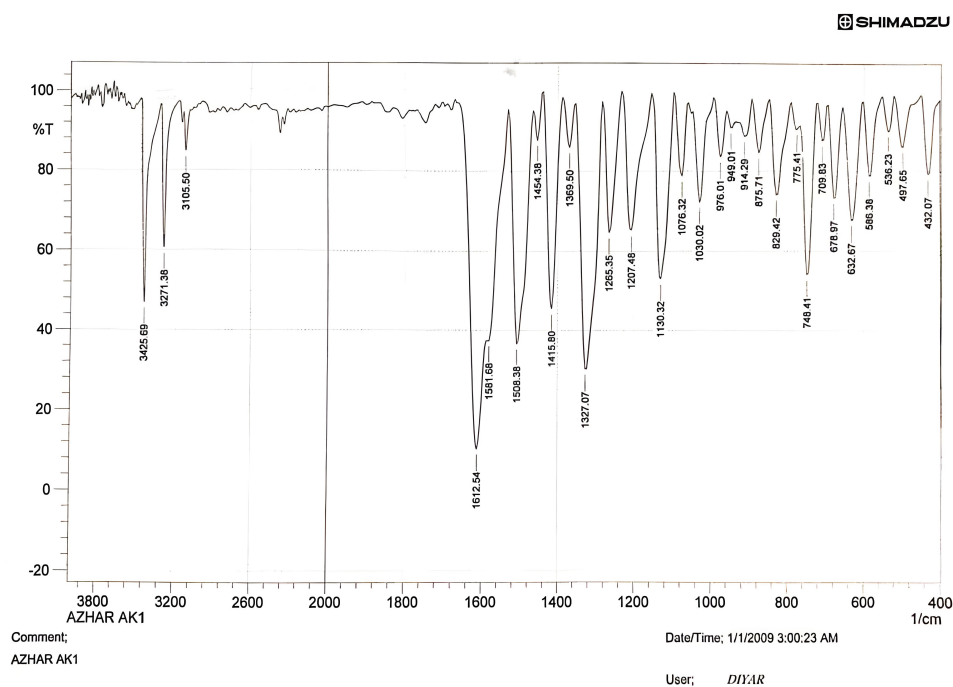
Hydrazone groups of all four compounds gave significant  $^1H$ NMR signals as singlet in the range 11.60-11.73 and 8.51-8.99 ppm referred to protons N-H and CH=N (Gomathi

**Table 1.** Physical Characteristics of the Compounds

Compound	mp °C	Colour	M.Wt.	Obtained %	TLC eluent	Rf
1a	298-300	Marron	275	88	Ether:Hexane 4:6	0.71
1b	264-266	Red	330	60	EtOH:Toluene 4:6	0.86
1c	236-238	Orange	346	65	EtOH:Hexane 6.5:3.5	0.91
1d	242-244	Yellow	332	83	DCM:EAC 4:6	0.87

**Table 2.** The Synthetic Compounds' FT-IR Data

Compound	$\nu(\text{OH})$	$\nu(\text{NH})$ hydra- zone	$\nu(\text{NH})$ Pyr- role	$\nu(\text{C-H})$ arom. str.	$\nu(\text{CH})$ alip. str.	$\nu(\text{C=O})$	$\nu(\text{C=N})$	$\nu(\text{C=C})$	$\nu(\text{N-O})$	$\nu(\text{C-O})$
1a	-	3425	3271	3105	-	-	1612	1581	1508 1327	-
1b	-	3421	-	3050	2951	-	1620	1589	1454 1390	1261 1134
1c	overlap	3400	-	3117	-	1666	1620	1504	1438 1385	1262
1d	3290	3400	-	3120	2935	-	1616	1516	1477 1327	1261

**Figure 2.** Compound 1a Spectrum in FT-IR

and Selvameena, 2022), respectively. Aromatic protons of 2,4-dinitrophenyl groups for all four compounds showed three signals, doublet signal at 8.85-8.86 ppm attributed to  $H_a$  proton with long range coupling  $J=2.6$  Hz of  $H_b$ . Doublet of doublet signals at the range 8.31-8.37 ppm for  $H_b$  proton coupled with  $H_a$  and  $H_c$  protons of  $J=2.6$  and 9.7 Hz, respectively.

Third signal as doublet appeared at the range 7.98-8.18 ppm referred to proton  $H_c$  coupled with  $H_b$  with  $J=9.7$  Hz, as shown in Table 3.

Compound 1a gave downfield singlet three signals between 6.18 and 7.05 ppm indicated to the aromatic protons of the pyrrole ring, while 11.58 was assigned to the NH Pyrrole

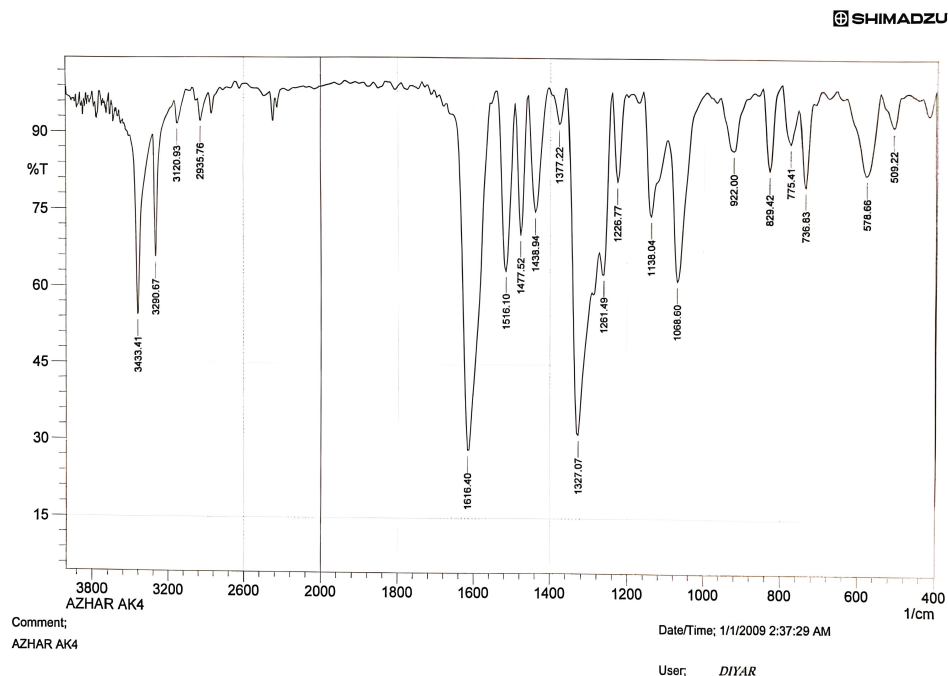


Figure 3. Compound 1d Spectrum in FT-IR

ring proton (Charles et al., 2020), Figure 4. Compound 1b showed aromatic signals at 7.45 ppm as singlet referred to proton  $H_f$ , doublet signal at 7.19 ppm for proton  $H_e$  coupled with  $H_d$  which gave doublet signal at 7.02 ppm ( $J=8.0$  Hz). Another singlet signal was appeared at 6.11 ppm attributed to two protons of methylene group which shifted to downfield field because of deshielding effect of neighboring oxygen atoms of dioxole ring, as shown in Figure 5.

Compound 1c gave three signals at 8.10, 8.04 and 7.07 ppm attributed to aromatic protons of salicylic fragment, singlet signal for  $H_f$  proton, doublet signal for  $H_d$  and doublet signal for  $H_e$ , respectively, ( $J_{d,e} = 9.2$  Hz), Figure 6. Compound 1d gave characteristic downfield singlet (9.52 ppm) and upfield singlet (3.83 ppm) signals attributed to protons -OH and -OCH<sub>3</sub> (Packialakshmi et al., 2022), respectively, of o-vanillin fragment. Protons with aromaticity in o-vanillin showed three signals, doublet signal at 7.44 ppm, doublet signal at 7.04 ppm, and triplet signal at 6.86 ppm referred to protons  $H_d$ ,  $H_f$ , and  $H_e$ , respectively, with coupling constant  $J=7.9$  Hz, as shown in Table 3 and Figure 7.

### 3.2 Potential Dynamic Polarization Measurements:

The electrochemical kinetics of metallic corrosion can be described by acquiring at least three polarizing parameters, such as corrosion current density ( $I_{corr}$ ), corrosion potential ( $E_{corr}$ ), and Tafel slopes ( $\beta_a$  and/or  $\beta_c$ ). To examine the corrosion behavior, utilize an E vs log I polarization curve. The polarization parameters (CR) are evaluated to determine the corrosion rate. As a result, it was possible to compute  $I_{corr}$  for the blank (solu-

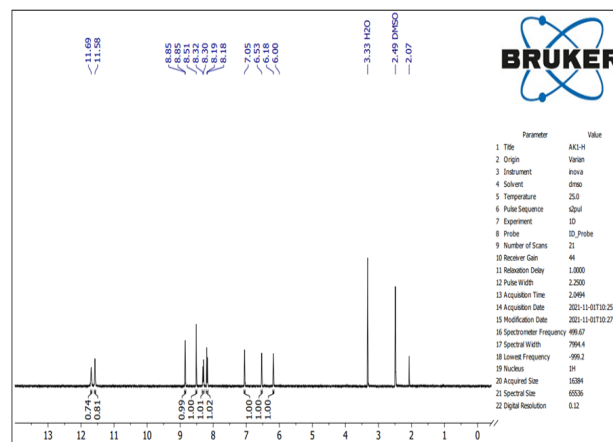
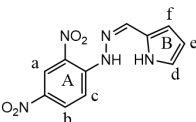
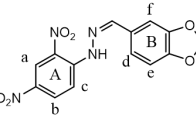
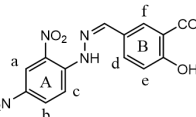
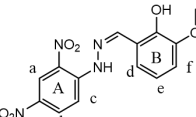


Figure 4. Spectrum of <sup>1</sup>H-NMR Compound 1a

tion devoid of inhibitor) and for all concentrations of all tested inhibitors, as shown in Figure 8. The electrochemical results are shown in Tables 4–7 and include the corrosion potential ( $E_{corr}$ ), corrosion current density (I), anodic and cathodic Tafel slopes, and inhibition efficiency (E%) (Kuraimid et al., 2023; Bouchart et al., 2019; Guo et al., 2022).

Cathodic polarization curves of acidic water rise to parallel Tafel lines, as illustrated in Figure 3 and Tables 4–7, demonstrating that the H<sub>2</sub> evolution reaction involves control activated. Thus, the existence of synthetic compounds has no bearing on how this process works, and generally speaking, adding different chemical concentrations results in a reduction

**Table 3.** <sup>1</sup>H-NMR Analysis of Produced Components

Compound	$\delta$ (ppm)					
	-NH-	-CH=N-	Arom. A	Arom. B	Others	
	11.69 (s)	8.51 (s)	8.85 (d) H <sub>a</sub> 8.31 (dd) H <sub>b</sub> 8.18 (d) H <sub>c</sub>	7.05 (s) H <sub>d</sub> 6.18 (s) H <sub>e</sub> 6.53 (s) H <sub>f</sub>	11.58 (s) -NH pyrrole ring	
	11.61 (s)	8.60 (s)	8.85 (d) H <sub>a</sub> 8.33 (dd) H <sub>b</sub> 8.12 (d) H <sub>c</sub>	7.02 (d) H <sub>d</sub> 7.19 (d) H <sub>e</sub> 7.45 (s) H <sub>f</sub>	6.11 (s) -CH <sub>2</sub> -	
	11.60 (s)	8.64 (s)	8.85 (d) H <sub>a</sub> 8.37 (d) H <sub>b</sub> 7.98 (d) H <sub>c</sub>	8.04 (d) H <sub>d</sub> 7.07 (d) H <sub>e</sub> 8.10 (s) H <sub>f</sub>		
	11.73 (s)	8.99 (s)	8.86 (d) H <sub>a</sub> 8.35 (dd) H <sub>b</sub> 8.03 (d) H <sub>c</sub>	7.44 (d) H <sub>d</sub> 6.86 (t) H <sub>e</sub> 7.04 (d) H <sub>f</sub>	9.52 (s) -OH 3.83 (s) -OCHH <sub>3</sub>	

ppm: part per million, s: singlet signal, d: doublet, dd: doublet of doublet, t: triplet

**Table 4.** The Corrosion Parameter Values for Mild Steel Corroding in 0.1M HCl with Galvanostatic Polarization in the Presence of Inhibitor 1a

Concentration	CR	$I_{cor}$ ( $\mu\text{A}/\text{cm}^2$ )	$E_{cor}$ (mV)	$\beta_c$ (mA/dm)	$\beta_a$ (mA/dm)	E %	$\theta$
0.00	3.383	504.7	-505.6	-113.1	95.2	-	-
$1 \times 10^{-5}$	2.227	167.2	-483.6	-117.2	90.4	69.23	0.6923
$1 \times 10^{-4}$	2.211	109.6	-472.1	-137.9	89.5	79.44	0.7944
$1 \times 10^{-3}$	1.812	97.4	-463.4	-130.5	75.3	80.70	0.8070

**Table 5.** The Corrosion Parameter Values for Mild Steel Corroding in 0.1M HCl with Galvanostatic Polarization in the Presence of Inhibitor 1b

Concentration	CR	$I_{cor}$ ( $\mu\text{A}/\text{cm}^2$ )	$E_{cor}$ (mV)	$\beta_c$ (mA/dm)	$\beta_a$ (mA/dm)	E %	$\theta$
0.00	3.383	504.77	-505.6	-113.1	95.2	-	-
$1 \times 10^{-5}$	1.984	104.70	-491.82	-115.3	96.1	89.9	0.899
$1 \times 10^{-4}$	1.880	85.40	-482.55	-105.8	104.9	83.08	0.8308
$1 \times 10^{-3}$	1.621	43.70	-471.23	-114.3	123.1	91.30	0.9134

**Table 6.** The Corrosion Parameter Values for Mild Steel Corroding in 0.1M HCl with Galvanostatic Polarization in the Presence of Inhibitor 1c

Concentration	CR	$I_{cor}$ ( $\mu\text{A}/\text{cm}^2$ )	$E_{cor}$ (mV)	$\beta_c$ (mA/dm)	$\beta_a$ (mA/dm)	E %	$\theta$
0.00	3.383	504.77	-505.6	-113.1	95.2	-	-
$1 \times 10^{-5}$	1.584	431.12	-451.68	-86.7	123.1	90.08	0.9008
$1 \times 10^{-4}$	1.580	419.45	-496.59	-87.9	117.2	90.60	0.9060
$1 \times 10^{-3}$	1.221	403.02	-481.62	-80.4	116.8	91.34	0.9130

in the density of currents. When the concentration rises, the cathodic Tafel slope ( $\beta_c$ ) remains unchanged. The findings show

that hydrogen reduction is prevented and that, as inhibitor concentration rises, inhibition efficiency increases as well, reaching



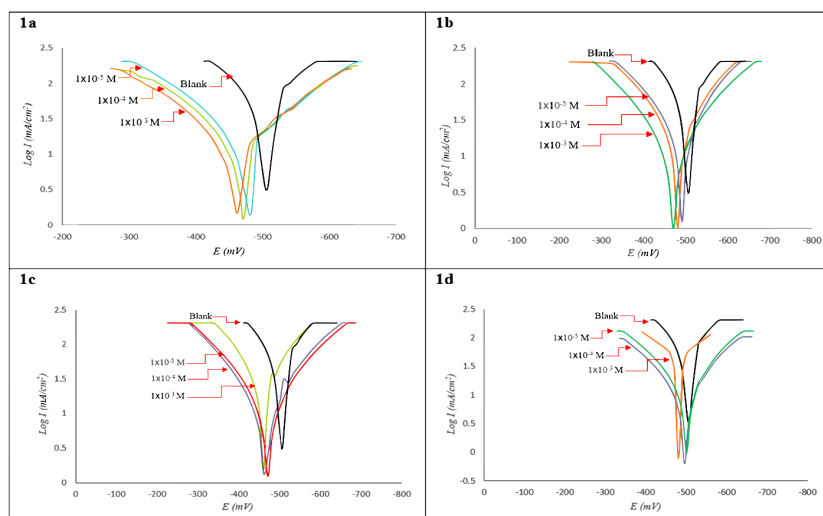


**Figure 8.** Tafel Graphs Showing the Anodic and Cathodic Polarization of Mild Steel in Acidic Conditions with and without Varying Inhibitor Concentrations at Room Temperature

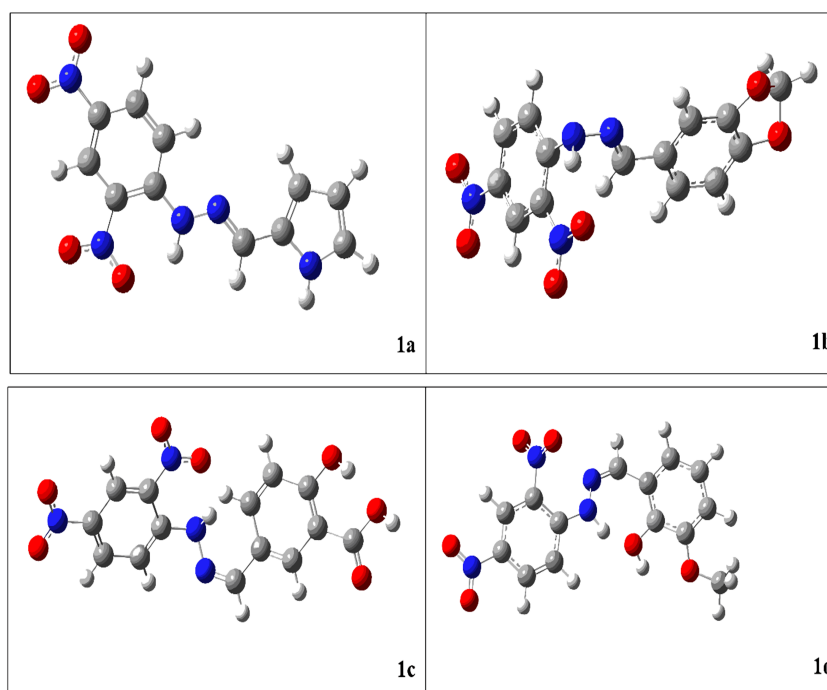


**Figure 9.** Optimized Geometrical Structures of Synthesized Compounds (1a-1d) by Gaussian

to acceptor molecules that have low energy empty molecules orbitals is indicated by high  $E_{HOMO}$  values. The process of transport across the adsorbed layer is influenced by the increasing values of the  $E_{HOMO}$ , which facilitates adsorption (Eduok, 2020; Adejoro et al., 2015).  $E_{LUMO}$  is a sign of The capability of a molecule to accept electrons. It is likely that a unit receive electrons increases with a lower value of  $E_{LUMO}$ .

As illustrated in Figure 10, the MOE program calculated the energy differential between  $LUMO$  and  $HOMO$  ( $\Delta E =$

$E_{LUMO}-E_{HOMO}$ ) as a variable, and the resulting lesser value in better molecule inhibition efficiency. Higher values will promote increase of corrosion inhibition for the dipole moment ( $\mu$ ) (Erteeb et al., 2021; Abdullah et al., 2021). It has been claimed that the best organic compounds for preventing corrosion are those that take in free electrons from the metal and transfer them to an anti-bonding orbital to form a feedback bond in addition to providing electrons to the metal's vacant d orbital.



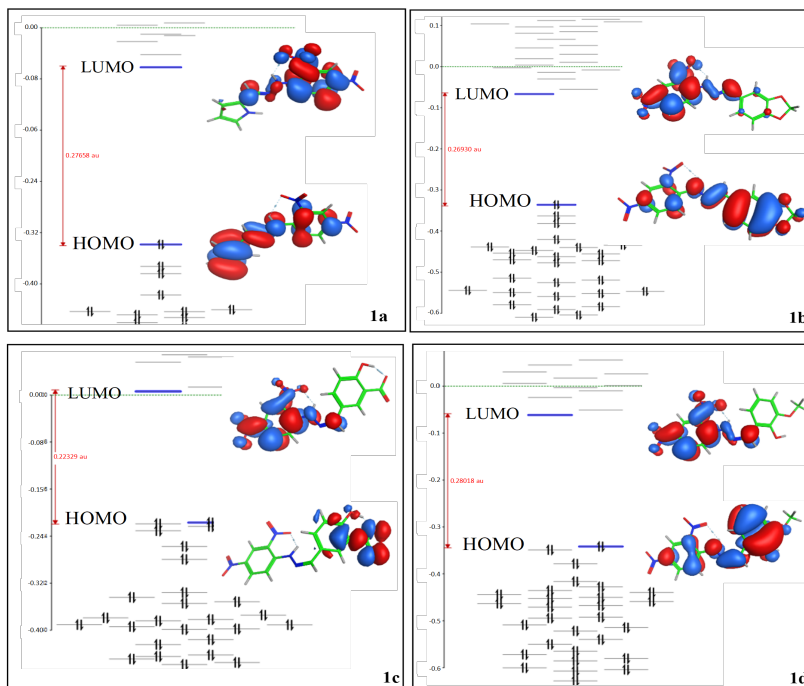


**Figure 10.** Frontier Molecular Orbitals and Energy Diagram of Title Compound by MOE Program

**Table 9.** Determined the Compounds' Quantum Chemical Characteristics by Hyperchem

Compound	$E_{HOM.}$	$E_{LUM.}$	$\Delta E$	Dipol.
1a	-9.353	-1.781	7.572	6.625
1b	-9.155	-1.742	7.477	7.534
1c	-9.029	-1.703	7.326	9.027
1d	-9.246	-1.535	7.711	8.894

**Table 10.** Determined the Compounds' Quantum Chemical Characteristics by Gaussian

Compound	$E_{HOM.}$	$E_{LUM.}$	$\Delta E$	Dipol.
1a	-9.432	-1.714	7.718	6.740
1b	-9.111	-1.900	7.211	7.682
1c	-8.805	-1.643	7.162	9.035
1d	-9.328	-1.413	7.915	8.812

Tables 8–10 show that 1c has the higher value of (10.325, 9.027, and 9.035 Debye) and the lower value of  $\Delta E$  (5.734, 7.326, and 7.162 eV) according to MOE, HyperChem, and Gaussian, respectively. This shows that there is good agreement between these values and the data on inhibition efficiency. Quantum chemical parameter data generally demonstrated the excellent inhibitory efficacy of these chemicals.

#### 4. CONCLUSION

It was possible to synthesis mild steel corrosion inhibitors, and spectroscopic methods allowed for a thorough structural analysis. Next, it was investigated how well they might stop stainless steel from corroding in a room-temperature 1.0 M HCl solution.. The inhibitors, namely (E)N-Benzo [1,3] dioxol-5-ylmethylene-N'-(2,4-dinitro-phenyl)- hydrazine (1b), (E)-5-((2-(2,4-dinitrophenyl)hydrazono)methyl)-2-hydroxybenzoic acid (1c), exhibited excellent corrosion inhibition performances, and highest inhibitor concentrations of  $1 \times 10^{-3}$  M, yielding inhibition efficiencies of 91.34% besides 91.30, respectively. From  $1 \times 10^{-5}$  M to the optimal concentration of  $1 \times 10^{-3}$  M, the inhibition efficacy rose as inhibitor concentration was increased. The connection between the inhibitors' electrical structures and their ability to stop corrosion efficiency was clarified by quantum chemistry simulations. When compared to other compounds, the 1c molecule has a strong inhibition efficiency and good performance as anti-corrosion agents. specifically due to its low energy band gap ( $\Delta E$ ) and high dipole moment ( $\mu$ ). The analyzed inhibitors' theoretical and experimental inhibition efficiency showed excellent agreement, supporting the validity of the process used.

#### 5. ACKNOWLEDGEMENT

The Department of Chemistry at the University of Basra's College of Education of Pure Science is acknowledged by the authors for its assistance with possible dynamic polarization measurements.

## REFERENCES

- Abdullah, R. S., A. El Nemr, S. S. El-Sakka, M. A. El-Hashash, and M. H. Soliman (2021). Synthesis of Phthalazinones with Amino or Hydrazide Moiety As Corrosion Inhibitors of Low Carbon Steel in 0.5 M H<sub>2</sub>SO<sub>4</sub>. *ChemistrySelect*, **6**(39); 10637–10647
- Adam, M. S. S., O. S. Abdel-Rahman, and M. M. Makhlof (2023). Metal Ion Induced Changes in the Structure of Schiff Base Hydrazone Chelates and Their Reactivity Effect on Catalytic Benzyl Alcohol Oxidation and Biological Assays. *Journal of Molecular Structure*, **1272**; 134164
- Adejoro, I., F. Ojo, and S. Obafemi (2015). Corrosion Inhibition Potentials of Ampicillin for Mild Steel in Hydrochloric Acid Solution. *Journal of Taibah University for Science*, **9**(2); 196–202
- Al-Amiery, A. A., W. N. R. W. Isahak, and W. K. Al-Azzawi (2023). Corrosion Inhibitors: Natural and Synthetic Organic Inhibitors. *Lubricants*, **11**(4); 174
- Argyropoulos, V., S. C. Boyatzis, M. Giannoulaki, E. Guilminot, and A. Zacharopoulou (2021). Organic Green Corrosion Inhibitors Derived from Natural And/or Biological Sources for Conservation of Metals Cultural Heritage. *Microorganisms in the Deterioration and Preservation of Cultural Heritage*, **5**; 341
- Bouchtart, A., M. Rguiti, K. E. Mouaden, A. Abourine, R. Salghi, and L. Bazzi (2019). Copper Corrosion Inhibition in Acetic Acid by Some Heteroatom Organic: Case of 1-Phenyl-5-Mercapto-Tetrazole. *Applied Journal of Environmental Engineering Science*, **5**(2); 183–192
- Charles, A., K. Sivaraj, and S. Thanikaikarasan (2020). Synthesis, Characterization and Corrosion Studies of Schiff Bases Derived from Pyrrole-2-Carbaldehyde. *Materials Today: Proceedings*, **33**(7); 3135–3138
- Chen, L., D. Lu, and Y. Zhang (2022). Organic Compounds As Corrosion Inhibitors for Carbon Steel in HCl Solution: A Comprehensive Review. *Materials*, **15**(6); 2023
- Deaf, H. K., E. Q. Jasim, H. Rafid, and K. Mohammed (2022). Synthesis, Corrosion Inhibition Study and DFT Calculation of Two New Azo Compounds. *Egyptian Journal of Chemistry*, **65**(12); 481–492
- Eduok, U. (2020). Theoretical Investigation of Molecular Properties of 5-Benzyl-6-Methyl Pyridazine-3-One and 5-Benzyl-6-Methyl Pyridazine-3-Thione and Their Potentials for Corrosion Inhibition for Steel. *International Journal of Electrochemical Science*, **15**(12); 12080–12102
- Elazabawy, O. E., O. A. El-Shamy, and N. E. El-Sattar (2023). Corrosion Inhibitory Characteristics, Thermodynamics, and Theoretical Studies of N-((2-Aminoethyl) Carbamothioyl) Acrylamide for Carbon Steel in 1 M HCl. *Egyptian Journal of Petroleum*, **32**(3); 7–14
- Erteeb, M., E. Ali-Shattle, S. Khalil, H. Berbash, and Z. Elshawi (2021). Computational Studies (DFT) and PM3 Theories on Thiophene Oligomers As Corrosion Inhibitors for Iron. *Am J Chem*, **11**; 1–7
- Gomathi, V. and R. Selvameena (2022). Synthesis, Structural Analysis and Antimicrobial Screening of Mn (II) Complexes of Schiff Bases. *Journal of the Mexican Chemical Society*, **66**(1); 70–78
- Guo, X., J. Wang, L. Huang, Y. Wang, L. Ma, D. Zhang, and L. Ma (2022). Corrosion Inhibition and Adsorption Process of 3-Amino-5-Mercapto-1, 2, 4-Triazole on Aluminium Alloy: Experimental and Theoretical Studies. *Frontiers in Materials*, **9**; 874899
- Hassan, A., M. S. Numin, K. Jumbri, K. E. Kee, N. Borhan, N. M. R. Nik Mohamed Daud, A. Mohammed Nor, M. F. Suhor, and R. Abdul Wahab (2023). Density Functional Theory Studies on New Possible Biobased Gemini Corrosion Inhibitors Derived from Fatty Hydrazide Derivatives. *ACS Omega*, **8**(26); 23945–23952
- Jabeen, M. (2022). A Comprehensive Review on Analytical Applications of Hydrazone Derivatives. *Journal of the Turkish Chemical Society Section A: Chemistry*, **9**(3); 663–698
- Jasim, E. Q., E. A. Alasadi, R. H. Fayadh, and M. A. Muhamman-Ali (2020). Synthesis and Antibacterial Evaluation of Some Azo-Schiff Base Ligands and Estimation the Cadmium Metal by Complexation. *Systematic Reviews in Pharmacy*, **11**(6); 677–687
- Jasim, E. Q., M. A. Ma, and R. H. Fayadh (2017). Synthesis and Characterization of Some Thiadiazole Compounds as New Corrosion Inhibitors for Mild Steel in Cooling Water. *Asian Journal of Chemistry*, **29**(11); 2361–2365
- Jasim, E. Q., M. A. Muhammad-Ali, and A. Almakki (2023). Synthesis, Characterization, and Antibacterial Activity of Some Mesalazine Derivatives. *Science and Technology Indonesia*, **8**(3); 338–343
- Kuraimid, Z. K., D. S. Abid, and A. E.-A. S. Fouda (2023). Synthesis and Characterization of a Novel Quaternary Ammonium Salt as a Corrosion Inhibitor for Oil-Well Acidizing Processes. *ACS Omega*, **8**(30); 27079–27091
- Lgaz, H., A. Chaouiki, M. R. Albayati, R. Salghi, Y. El Aoufir, I. H. Ali, M. I. Khan, S. K. Mohamed, and I.-M. Chung (2019). Synthesis and Evaluation of Some New Hydrazones As Corrosion Inhibitors for Mild Steel in Acidic Media. *Research on Chemical Intermediates*, **45**; 2269–2286
- Maniak, H., M. Talma, and M. Giurg (2021). Inhibitory Potential of New Phenolic Hydrazide-Hydrazones with a Decoy Substrate Fragment Towards Laccase from a Phytopathogenic Fungus: SAR and Molecular Docking Studies. *International Journal of Molecular Sciences*, **22**(22); 12307
- Mazlan, N., K. Jumbri, M. A. Kassim, R. A. Wahab, and M. B. A. Rahman (2022). Density Functional Theory and Molecular Dynamics Simulation Studies of Bio-Based Fatty Hydrazide-Corrosion Inhibitors on Fe (1 1 0) in Acidic Media. *Journal of Molecular Liquids*, **347**; 118321
- Muhammad, A. A., T. A. Nyijime, and A. S. Muhammad (2020). Density Functional Theory and Molecular Dynamic Simulation Studies on the Corrosion Inhibition of Some Thiosemicarbazide Derivatives on Aluminum Metal. *Journal of Applied Surfaces and Interfaces*, **8**(1-3); 7–14

- Muhammad-Ali, M. A., E. Q. Jasim, and A. H. Al-Saadoon (2023). Synthesis, Antibacterial Evaluation, and Docking Studies of Some Azo Compounds and Schiff Bases Derived from Sulfonamide. *Journal of Medicinal and Chemical Sciences*, **6**(9); 2128–2139
- Njong, R. N., B. N. Ndosiri, E. N. Nfor, and O. E. Offiong (2018). Corrosion Inhibitory Studies of Novel Schiff Bases Derived from Hydralazine Hydrochloride on Mild Steel in Acidic Media. *Open Journal of Physical Chemistry*, **8**(1); 15–32
- Obot, I., A. A. Bahraq, and A. H. Alamri (2022). Density Functional Theory and Molecular Dynamics Simulation of the Corrosive Particle Diffusion in Pyrimidine and Its Derivatives Films. *Computational Materials Science*, **210**; 111428
- Oukhrib, R., Y. Abdellaoui, A. Berisha, H. Abou Oualid, J. Halili, K. Jusufi, M. Ait El Had, H. Bourzi, S. El Issami, and F. A. Asmary (2021). DFT, Monte Carlo and Molecular Dynamics Simulations for the Prediction of Corrosion Inhibition Efficiency of Novel Pyrazolynucleosides on Cu (111) Surface in Acidic Media. *Scientific Reports*, **11**(1); 3771
- Oyeneyin, O. E., N. D. Ojo, N. Ipinloju, E. B. Agbaffa, and A. V. Emmanuel (2022). Investigation of the Corrosion Inhibition Potentials of Some 2-(4-(substituted) Arylidene)-1H-Indene-1, 3-Dione Derivatives: Density Functional Theory and Molecular Dynamics Simulation. *Beni-Suef University Journal of Basic and Applied Sciences*, **11**(1); 1–14
- Packialakshmi, P., P. Gobinath, D. Ali, S. Alarifi, R. Gurusamy, A. Idhayadhulla, and R. Surendrakumar (2022). New Chitosan Polymer Scaffold Schiff Bases As Potential Cytotoxic Activity: Synthesis, Molecular Docking, and Physicochemical Characterization. *Frontiers in Chemistry*, **9**; 796599
- Parvarinezhad, S. and M. Salehi (2021). Synthesis, Characterization, Anti-Proliferative Activity and Chemistry Computation of DFT Theoretical Methods of Hydrazine-Based Schiff Bases Derived from Methyl Acetoacetate and  $\alpha$ -Hydroxyacetophenone. *Journal of Molecular Structure*, **1225**; 129086
- Raczuk, E., B. Dmochowska, J. Samaszko-Fiertek, and J. Madaj (2022). Different Schiff Bases—Structure, Importance and Classification. *Molecules*, **27**(3); 787
- Sharma, P., D. Sharma, A. Sharma, N. Saini, R. Goyal, M. Ola, R. Chawla, and V. Thakur (2020). Hydrazone Comprising Compounds As Promising Anti-Infective Agents: Chemistry and Structure-Property Relationship. *Materials Today Chemistry*, **18**; 100349
- Vhanale, B. T., N. J. Deshmukh, and A. T. Shinde (2019). Synthesis, Characterization, Spectroscopic Studies and Biological Evaluation of Schiff Bases Derived from 1-Hydroxy-2-Acetonaphthanone. *Helvion*, **5**(11); 1–19
- Zhang, D., W. Zhao, Z. Feng, Y. Wu, C. Huo, L. He, and W. Lu (2019). Preparation of Polymer–Rare Earth Complexes Based on Schiff-Base-Containing Salicylic Aldehyde Groups Attached to the Polymer and Their Fluorescence Emission Properties. *e-Polymers*, **19**(1); 15–22